NANO MATERIALS Cite This: ACS Appl. Nano Mater. 2018, 1, 1430–1437

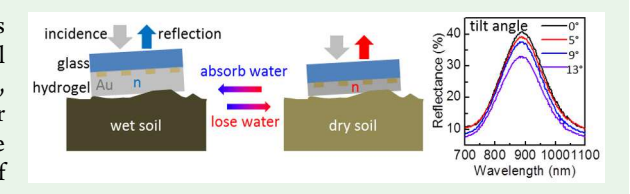
www.acsanm.org

Angle-Independent Optical Moisture Sensors Based on Hydrogel-**Coated Plasmonic Lattice Arrays**

Wenxiang Chen,^{†®} Gaoxiang Wu,^{‡®} Mingliang Zhang,[†] Nicholas J. Greybush,^{‡®} Jordan P. Howard-Jennings, Naixin Song, F. Scott Stinner, Shu Yang, and Cherie R. Kagan*, Asian Song, Shu Yang, Shu

Supporting Information

ABSTRACT: Plasmonic nanostructures provide excellent platforms for colorimetric sensors in chemical, biological, and environmental applications. In contrast to the existing library of plasmonic sensors, we report an angle-independent optical sensor that is designed for monitoring soil moisture and operating on rough surfaces. The optical moisture sensor is constructed by coating hydrogel on top of an ultrathin, plasmonic Au nanorod lattice array, where the refractive



index changes of the hydrogel upon exposure to moisture are transduced into spectral shifts of the resonances of the array. A modified Langmuir adsorption isotherm model is used to capture the dynamics of water adsorption and desorption at the interface between the sensor and the ambient environment. The nanorod length and the nanorod array pitch are systematically tuned to decouple the localized surface plasmon resonance of the nanorods and the Rayleigh anomalies of the nanorod array, creating sensors with angle-independent resonances (~ 0.2 nm/deg). As a proof of concept, we place the sensor on uneven soil surfaces and demonstrate the consistent sensor resonance shift that only depends on the soil wetness. Robust, eco-friendly optical moisture sensors with angle-independent resonances provide a promising sensing platform for smart soil moisture monitoring important to tackle the challenge of water scarcity in agriculture.

KEYWORDS: optical moisture sensor, angle-independent resonance, surface lattice resonance, soil moisture monitoring, water scarcity

1. INTRODUCTION

Growing water scarcity is one of the world's leading challenges to sustainable food production according to the United Nations Food and Agriculture Organization. Agricultural water withdrawal accounts for 70% of the global sum of all water use.² To better manage agricultural water usage, professionals have developed different methods for gathering soil moisture information. Most commercial moisture sensors are electrically powered, which include time domain reflectometry, 3,4 time domain transmission, 5,6 and capacitance sensors. Despite their accuracy, these sensors require power supplies and only provide point measurements, making them difficult to implement across large, hundred-acre area fields for agricultural purposes.^{6,8-10}

Optical sensors based on photonic crystals or plasmonic nanostructures have reported spontaneous, vivid color variations upon exposure to moisture, which provide excellent sensor platforms for operation across large-area fields. Many groups have developed optical moisture sensors based on photonic crystals in the form of either inverse opal structures or close-packed supraballs made of hydrophilic polymers. 11-18 Upon exposure to moisture, the lattice constant and the refractive index (RI) of the photonic crystals change, leading to the variation of visible colors. On the other hand, top-down fabrication and bottom-up chemical synthesis have been used to tailor the size and shape of metallic nanostructures to create plasmonic colorimetric sensors that have been extensively used in chemical, biological, and environmental applications. 19

The sensing mechanism is based on the selective adsorption of analytes near or on the metallic nanostructures which results in a change in the RI of the surroundings and therefore a shift in the localized surface plasmon resonance (LSPR). For example, various humidity-sensitive materials, such as hydrogel, mercaptopoly(ethylene glycol) (mercaptoPEG), and poly(Nisopropylacrylamide) (PNIPAm) brush, have been ligated to or coated on plasmonic nanostructures for moisture sensing.²⁷ For better sensitivity, the plasmonic nanostructure arrays are tuned in size and shape to enable the coupling between the LSPR and Rayleigh anomalies to generate sharp resonances.²²

To date, optical moisture sensors based on photonic crystals and plasmonic nanostructures have been mostly investigated for high sensitivity and/or short response time, with little attention paid to the angular variations of the sensor resonances. The demonstrated vivid colors of photonic crystals characteristically have large angular variations due to diffraction, while plasmonic nanostructure arrays with hybridized resonances also suffer from a large angle dependence due to the coupled Rayleigh anomalies (diffractive orders). 22,34,35 For applications such as environmental monitoring where the soil surface is rough and the ground profile varies, it is important for optical sensors to possess angle-independent resonances that

Received: February 24, 2018 Accepted: March 6, 2018 Published: March 6, 2018



[†]Department of Electrical and Systems Engineering, [‡]Department of Materials Science and Engineering, and [§]Department of Chemistry, University of Pennsylvania, Philadelphia, Pennsylvania 19104, United States

are insensitive to extraneous perturbations in order to guarantee the accuracy of optical sensing data.

In this work, we experimentally and computationally design and characterize hydrogel-coated, plasmonic Au NR lattice arrays as a platform to create passive optical moisture sensors with angle-independent resonances. The sensor responses to a wide range of relative humidity (RH) are captured and fitted by a generalizable model, which provides fundamental understanding of water adsorption and desorption on the sensor surface and an analytical solution for the temporal evolution of the sensor responses. By tailoring the NR length (30-350 nm) and the pitch of the array (400-1000 nm) in experiments and finite-difference time domain (FDTD) simulations, we investigate the relationship between the angular variations of the plasmonic sensor resonances and the dimensions of the NR array. More specifically, we identify NR array designs in which the LSPR of the individual NRs and the diffractive orders present in the periodic array are decoupled, realizing sensors with angle-independent resonances (~0.2 nm/deg). We further place the sensor on the soil surface and demonstrate the consistent resonance shift that depends on the soil wetness and that is independent of tilting of the sensor caused by the soil roughness. Eco-friendly, plasmonic moisture sensors with angle-independent resonances promise a "smart" solution for soil moisture monitoring and therefore efficient water management in agriculture.

2. RESULTS AND DISCUSSION

Fabrication of Optical Moisture Sensors. The fabrication of the hydrogel-coated, Au NR array optical moisture sensor is shown in Figure 1a, and details can be found in the

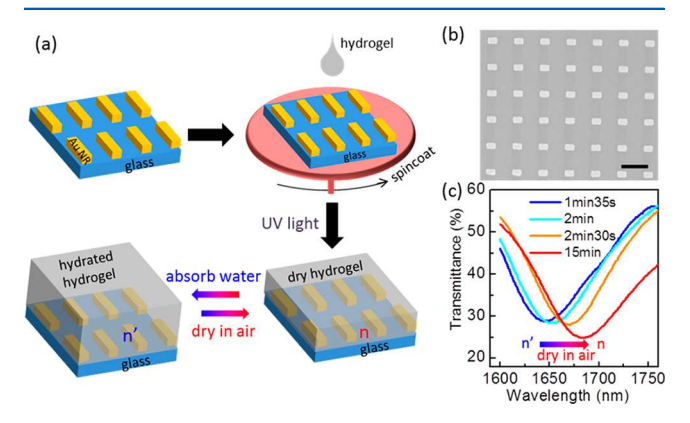


Figure 1. (a) Schematic of the hydrogel-coated, Au NR array optical moisture sensor fabrication process. (b) SEM image of the array of Au NRs with 362 \pm 4 nm length, 238 \pm 3 nm width, and 32 \pm 1 nm thickness on a 1000 nm pitch. The scale bar is 1 μ m. (c) Transmittance spectra for a hydrogel-coated, Au NR array optical moisture sensor as a function of time after it is removed from water and placed in air (RH = 30% and T = 23 °C).

Experimental Section. We choose electron-beam lithography and Au thermal evaporation to prototype sensor designs. Figure 1b shows a scanning electron microscope (SEM) image of an example array of Au NRs that are 362 ± 4 nm in length, 238 ± 3 nm in width, and 32 ± 1 nm in thickness repeated on a 1000 nm pitch (thickness is measured by atomic force microscopy (AFM) in Supporting Information Figure S1a,b). The corresponding transmittance spectrum of the pristine Au NR array, before spin coating of hydrogel, has a resonance at 1532

nm (Figure S1c). Hydrogel films of 640 nm thickness are deposited on top of the Au NR arrays via spin-coating (Figure S1d,e). We use this design to characterize the sensor response to different RH environments to study the sensing mechanism and then vary the NR length (30–350 nm) and array pitch (400–1000 nm) to define design rules to create sensors that minimize the angle dependence of their optical responses.

Characterization of the Dynamic Sensor Responses with Water Content. To characterize the response of the sensors as a function of their water content, we soak the sensors in water and take them out and measure their transmittance as a function of time as the water evaporates in air at a constant RH and temperature (T). Air RH is measured by a commercial humidity sensor integrated in the measurement setup (Figure S2). Figure 1c shows the responses of the sensor as the water in the hydrogel evaporates at RH = 30% and T = 23 °C. Since water has a lower refractive index (RI, n = 1.33) than pure hydrogel (n = 1.45), the effective RI of the hydrogel increases as water evaporates, resulting in a red-shift of the resonance $(\Delta \lambda)$ of the Au NR array from 1646 to 1685 nm. From fully soaked to dry, the sensor resonance maintains a similar transmittance amplitude of 33.5 \pm 2.1% and also a similar full width at half-maximum (fwhm) of 118 ± 25 nm.

To confirm the operating mechanism of the sensor, we correlate the spectral shift of the resonance of the Au NR array with the water content in the hydrogel. The water content is characterized by integrating the water fingerprint regions (2530–3845 cm⁻¹) in transmittance spectra of the sensor collected using Fourier transform infrared (FTIR) spectroscopy (Figure S3). The red-shift in the resonance of the sensor maps the decrease in water content in the sensor (Figure 2a).

We characterize the sensor response to environments of different RH (i.e., moisture content). In experiment a fully soaked sensor is held in air of different RH, and its resonance is monitored as water evaporates until the sensor reaches steady

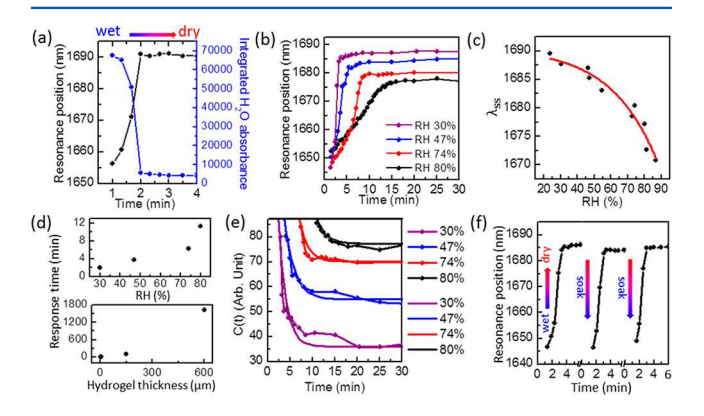


Figure 2. (a) Time-dependent sensor resonance positions and integrated intensity of the water stretch region (2530–3845 cm⁻¹) in FTIR spectra of the optical moisture sensor, as it dries over time from the fully soaked in water to RH = 3% and T = 23 °C. (b) Sensor resonance position as a function of drying time from fully soaked in water to steady state in 30%, 47%, 74%, and 80% RH air. (c) Steady-state resonance positions (λ_{ss}) in different static RH environments. (d) [top] Sensor response time extracted from resonance position curves in (b); [bottom] and the response time for sensors with different thickness hydrogel films. (e) Resonance position curves in (b) are converted to concentration of water (dotted lines) based on eq 1 and Supporting Information eq S3. Time-dependent concentration curves are fit to eq 2 (solid lines). (f) Sensor resonance position for three cycles of soaking in water and drying in 30% RH air.

state (Figure 2b). The steady-state resonance position (λ_{ss}) as a function of RH is plotted in Figure 2c (black dots). As RH increases from 24% to 87%, the sensor λ_{ss} shifts from 1688.7 \pm 2.3 to 1670.9 \pm 2.3 nm. We fit the λ_{ss} dependence on RH by an empirical function

$$\lambda_{\rm ss} = \lambda_{\rm ss}({\rm RH} = 0) - \Delta \lambda' \exp\left(-\frac{1 - {\rm RH}}{B}\right)$$
 (1)

where B=0.27 is a constant related to both the moisture absorbing ability of the hydrogel and the NRs' sensitivity to the environmental RI change, $\lambda_{\rm ss}({\rm RH}=0)=1690.6$ nm is the resonance wavelength at approximately RH = 0 [since $\lambda_{\rm ss}({\rm RH}=0)\gg\Delta\lambda'\exp\left(-\frac{1}{B}\right)]$, and $\Delta\lambda'=31.8$ nm is approximately the resonance variation from RH = 0 to 100%. $\Delta\lambda'$ is consistent with theoretical predictions of the resonance shift with similar variation in the RI of the surroundings for Au nanobar arrays. The standard deviation in measured RH is 4.5% RH, noting that the commercial humidity reference sensor RH accuracy is 2% and experimentally limits the RH determination of the optical moisture sensor.

The response time, conventionally defined as the time needed for a fully soaked sensor to reach 90% of λ_{ssr}^{37} is calculated from Figure 2b and increases from 1.9 to 11.3 min as the air RH increases from 30% to 80% (upper panel of Figure 2d). A two-stage model is used to explain the temporal evolution of the sensor responses (Figure 2b is enlarged in Figure S4 to highlight each stage). In stage I, water inside the hydrogel evaporates into air, the hydrogel shrinks in thickness, and the resonance shifts toward longer wavelengths. In stage II, the resonance position gradually approaches its RH-dependent steady-state wavelength. The water remaining inside the hydrogel becomes a minority component, and the hydrogel thickness remains unchanged. Since water in higher RH environments evaporates more slowly, the slope of the resonance curve for higher RH is smaller.

An analytical model, which explicitly illustrates the submicroscopic processes of water adsorption and desorption at the interface between hydrogel and air, is found to describe the time-dependent sensor responses. We use the widely acknowledged Langmuir adsorption isotherm model, which is conventionally used to characterize the adsorption of an ideal gas on a two-dimensional surface with equivalent binding sites, with modifications that account for the transport of moisture inside hydrogel to fit our experimental results. In stage II, since the thickness of hydrogel can be approximated as constant, the time-dependent water concentration in the hydrogel film has an analytical solution derived from the modified model (derivation in Supporting Information):

$$C(t) = C_{\rm ss} + (C_0 - C_{\rm ss}) \exp\left(-\frac{k_{\rm off}}{h}t\right)$$
 (2)

where constants $C_{\rm ss}$ and C_0 are respectively the concentrations of water in hydrogel film at steady state and the value found by extrapolating C(t) to t=0, h is the thickness of the hydrogel film, and $k_{\rm off}$ is the water desorption rate constant multiplied by the thickness of the interfacial layer of hydrogel that adsorbs water molecules from the air.

To test the suitability of this model to describe the timedependent sensor responses in different RH environments, we relate the resonance position of the sensor to RH by eq 1 and then to the concentration of water (shown in Figure 2e) (derivation in Supporting Information). We fit our model to the experimental data, with fitting parameter $k_{\rm off}=0.34\pm0.06~\mu{\rm m~s}^{-1}$ for different RH conditions from 30% to 80% (details in Supporting Information). The consistency of the fit to the experimental results and the similar constant $k_{\rm off}$ obtained from different RH conditions suggest that the time evolutions of the sensor responses obey the modified Langmuir adsorption isotherm model. The analytical solution indicates that the water concentration in the sensor decays exponentially with a time constant of $1/\left(\frac{k_{\rm off}}{h}\right)$ (eq 2).

We construct optical sensors with varying hydrogel film thickness: 640 nm, 150 μ m, and 600 μ m without changing the NR array dimensions (150 and 600 μ m hydrogel film thickness are measured by a pair of calipers). For different hydrogel film thickness, the sensors show a similar steady-state resonance of 1700 ± 11 nm and resonance shift of 42 ± 2 nm, suggesting that the thickness of hydrogel has little influence over the plasmonic resonance features (Figures S5 and S6). However, the response time for a fully soaked sensor to reach steady state in 30% RH air varies by 3 orders of magnitude, from 2 to 90 min and then 1624 min as the hydrogel thickness increases (Figure 2d, bottom panel, and Figure S6). Thicker hydrogel films significantly increase the migration distance of water molecules³⁸ and the amount of water that can be contained inside the hydrogel, contributing to a much longer response time, which is consistent with eq 2 derived from Langmuir adsorption isotherm model. In the experiments described below, we use the thinnest hydrogel film (640 nm) we realize by spin-coating at the highest rate (8000 rpm), providing sensors with a reasonable response time of \sim 2 min. While faster response times are achievable by replacing the hydrogel film with a thinner polymer brush, for example, 20 nm PNIPAm,³³ these time scales are not required for applications in soil moisture monitoring.

The repeatability of the sensor response is tested by cyclically soaking the sensor in water three times and allowing it to reach steady state in air of 30% RH (Figure 2f). The three measurement cycles have similar fully soaked and steady-state resonance positions. There is a 1.4 nm variation in the resonance position in the fully soaked state, which is due to slightly different amounts of water contained in the hydrogel when the measurements started. Furthermore, we note that the swelling of this synthetic hydrogel has negligible temperature dependence near room temperature.³⁹

2.3. Design of Plasmonic Lattice Arrays To Tailor Angle Dependence of the Sensor. We present a variety of Au NR array designs to study the relationship between the dimensions of the Au NR array and the angle dependence of the sensor resonance. The Rayleigh anomaly arises from the superposition of the LSPR of the individual NRs and the diffractive orders that propagate parallel to the substrate surface, which yields sharp and highly angle-sensitive optical resonances. On the contrary, separating the LSPR and the diffractive orders in wavelength can yield resonances that are only created by the LSPR and are therefore independent of the incident angle of light. In the case of Au NRs in a square lattice array, for light at normal incidence, the wavelengths of the diffractive orders that propagate parallel to the substrate surface are expressed as 35

$$\lambda_{\rm D} = dn_{\rm sub}/m \tag{3}$$

ACS Applied Nano Materials Article

$$\lambda_{\rm D} = dn_{\rm med}/m \tag{4}$$

where d is the pitch of the square lattice array and n_{sub} and n_{med} are the RI of the substrate and the ambient medium (hydrogel). Equations 3 and 4 are for diffractive orders propagating in the substrate and in the ambient medium, respectively.

We compute the steady-state resonance wavelength of the sensor (λ_{ss}) as a function of the NR length and the pitch of the lattice array via the FDTD method (Figure 3a). We plot the

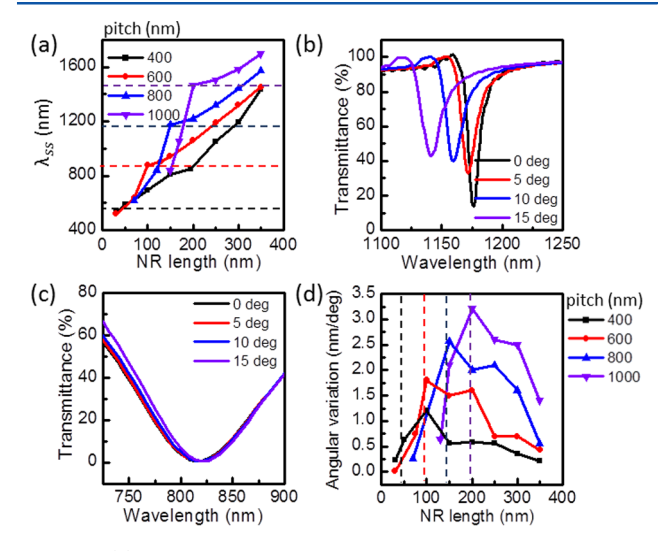


Figure 3. (a) FDTD simulations of the steady-state resonance position (λ_{ss}) at RH = 30% for optical moisture sensors as a function of NR length for different NR array pitches: 400 nm (black), 600 nm (red), 800 nm (blue), and 1000 nm (purple). The NR width is 200 nm, and the thickness is 32 nm. The straight dashed lines indicate the first-order, substrate-mode $\lambda_{\rm D}$ at different NR array pitches: 400 nm (black), 600 nm (red), 800 nm (blue), and 1000 nm (purple). Transmittance spectra for an array of Au NRs at 200 nm diameter and 32 nm thickness on a (b) 800 nm pitch and a (c) 400 nm pitch for light incident at various angles: 0° (black), 5° (red), 10° (blue), and 15° (purple). (d) Angular variation of the sensor resonance as a function of the NR length and NR array pitch. The vertical dashed lines indicate the NR lengths where $\lambda_{\rm D}$ equals λ_{ss} at different NR array pitch: 400 nm (black), 600 nm (red), 800 nm (blue), and 1000 nm (purple).

first-order, substrate-mode $\lambda_{\rm D}$ (dashed lines) together with $\lambda_{\rm ss}$ to show its superposition with the sensor resonance, where the Rayleigh anomaly occurs. It is worth mentioning that for higher order $\lambda_{\rm D}$ the anomalies appear at shorter wavelengths where the resonance amplitude is low and therefore not considered for sensor applications.

The angle dependence of the sensor resonance is simulated for various NR lengths and array pitches. To give an example of sensors in on-resonance and off-resonance conditions of the LSPR with the diffractive orders, we show the transmittance spectra of the sensor at different incident angles $(0^{\circ}-15^{\circ})$ for Au NRs of 200 nm diameter and 32 nm thickness on a 800 nm pitch and a 400 nm pitch square lattice array (Figure 3b,c). We define the angular variation of the sensor resonance as the maximum resonance variation divided by the corresponding change in angle for the incident light. It is 2.3 nm/deg for the angular variation for the Au NR array with a 800 nm pitch, while it is 0.2 nm/deg for that of the Au NR array with a 400 nm pitch. We summarize the angular variations of the sensor resonances in Figure 3d. The on-resonance NR lengths, where

 $\lambda_{\rm D}$ overlaps $\lambda_{\rm ss}$, are marked with dashed lines to illustrate the large angle dependence created by the Rayleigh anomaly. On the contrary, when the $\lambda_{\rm D}$ is separated from the $\lambda_{\rm ss}$ (off-resonance), i.e., the NR lengths are away from the on-resonance NR lengths, the angle dependence of the sensor resonance gradually decreases since the LSPR is angle insensitive.

Experimentally we fabricate sensors in the on- and off-resonance conditions according to the Au NR array designs in Figure 3b,c. Experimental transmittance and reflectance spectra of the on-resonance sensor at steady state of RH = 30% are presented in Figure 4a. In the transmittance spectrum collected

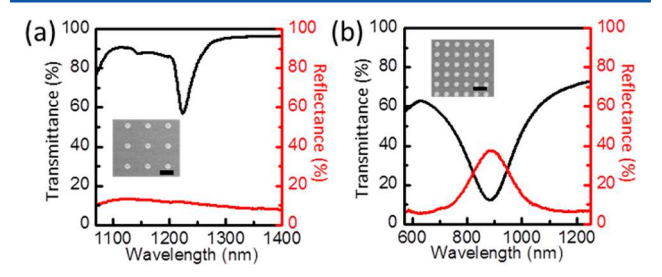


Figure 4. Transmittance (black) and reflectance (red) spectra of a sensor with (a) Au NRs 197 ± 6 nm diameter and 32 nm thickness on a 800 nm pitch and (b) 193 ± 4 nm diameter and 32 nm thickness on a 400 nm pitch. Transmittance spectra are collected at normal incidence, and the reflectance spectra are collected through an objective with NA = 0.7. Insets show SEM images of the Au NR arrays. Scale bar = 500 nm.

at normal incidence, the sensor resonance is at 1220 nm and has a 40 nm fwhm. However, resonances are not observable in the reflectance spectrum that is collected within $\pm 45^{\circ}$ through an objective. It suggests that there is a large angular variation in the sensor resonance which obscures the resonance feature in the reflectance spectrum that is collected from a wide range of reflection angles. In contrast, a pronounced sensor resonance in the off-resonance condition is observed in both transmittance and reflectance spectra (Figure 4b). The resonance peak in the reflectance spectrum is centered at 889 nm and has a fwhm of 167 nm, consistent with the resonance in the transmittance spectrum at 885 nm with a fwhm of 195 nm.

More sensor parameters are computed and experimentally demonstrated for a more comprehensive understanding of sensor performance (Figures S7–S9), including the sensor resonance variation ($\Delta\lambda$ from fully soaked to dry states at RH = 30%), the fwhm of the sensor resonance (at RH = 30%), and the ratio between the $\Delta\lambda$ and the fwhm which characterizes the resolution of the sensor. It should be pointed out that the fwhm of the sensor increases as the sensor design shifts from onresonance to off-resonance, which limits the resolvability of the resonance peaks. Different shaped plasmonic nanostructures, for example, nanoholes and nanovolcanos, could be investigated in the off-resonance conditions to achieve smaller fwhm. 22,25,33

Motivated by the need to operate on the uneven soil surface which inevitably causes the optical sensor to tilt at random angles, we select an off-resonance sensor (nanodot array sensor in Figure 4b) to demonstrate soil moisture monitoring as a proof of concept (Figure 5a). The moisture sensor is put on a series of soil samples containing 56, 27, and 10 wt % water, with the hydrogel side in contact with the soil (Figure 5b–d). We collect reflectance instead of transmittance spectra of the sensor

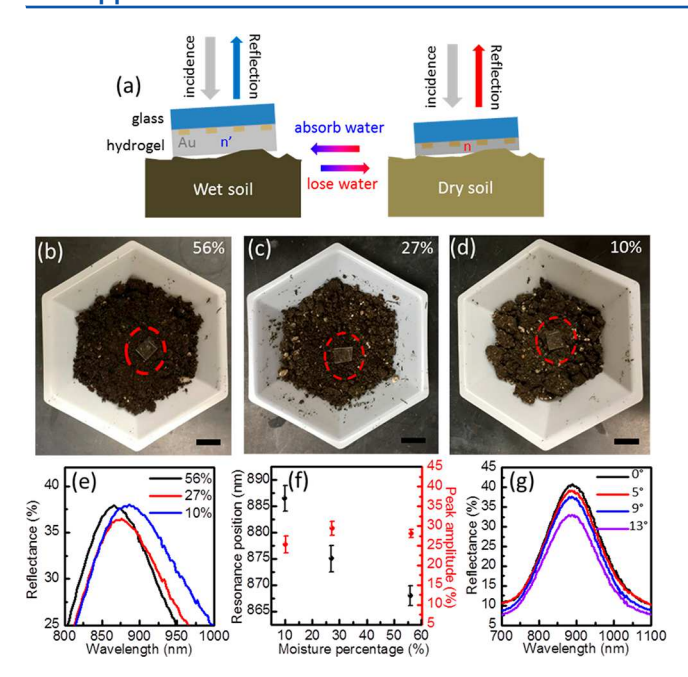


Figure 5. (a) Schematic of sensor operation on wet and dry soil. The refractive index of hydrogel changes according to the soil wetness, resulting in different reflection spectra of the sensor in near-infrared. (b-d) Photographs of hydrogel-coated, Au NR array optical moisture sensor (marked by red dashed circle) placed in contact with soil samples having 56 wt % (b), 27 wt % (c), and 10 wt % (d) moisture, respectively. Scale bar = 1 cm. (e) Average reflectance spectra from three measurements of the sensor on top of each soil sample. (f) Position (black dots) and amplitude (red dots) of the sensor resonance from the averaged spectra. (g) Reflectance spectra for the sensor as it is tilted at 0° (black), 5° (red), 9° (blue), and 13° (purple) to the horizontal plane.

as the soil is not transparent in the near-infrared. The sensor resonance position (Figure 5e and Figure S10) shifts from 868 \pm 2 to 887 \pm 2 nm as the water weight percentage of soil decreases from 56 to 10 wt %. The sensitivity of the sensor is described by the resonance shift of 0.4 nm per 1 wt % soil moisture variation. We note that the resonance shift in reflectance spectra coincides with that in transmittance spectra where the resonance shifts from 868 to 885 nm (Figure S8d), which ensures that consistent sensor signals can be obtained from both reflectance and transmittance measurements. The reflectance peak amplitude of the sensor is maintained at 27.6 \pm 2.1% for measurements on different soil samples (Figure 5f and Figure S11), stronger than that of a monolayer of the photonic crystals. 13 We tilt the sensor from 0° to 13° relative to the horizontal plane to test for any variation in the reflectance spectrum (Figure 5g). This range of angles is selected since agricultural fields, which can have a root-mean-square roughness in surface height of 3 cm and a correlation length of 30 cm, 41 are estimated to cause random tilting of the sensor in the range of 0°-6°. The resonance position remains unchanged at 889 ± 1 nm (0.2 nm/deg) for tilting angles between 0° and 13°, indicating the sensing data are independent of the soil surface roughness. The resonance amplitude varies slightly between $29.7 \pm 2.3\%$ as the incident angle changes, which we hypothesize arises from a small decrease in the light reflected from the glass substrate and collected by the lens when the sensor is tilted. It should be noted that other than the sensor design in Figure 4b, there are other choices of sensors that operate in off-resonance conditions and could be used

according to design rules in Figure 3d. For example, an array of Au NRs that are 350 nm in length, 200 nm in width, 32 nm in thickness, and on an 800 nm pitch has a resonance at longer wavelengths of 1573 nm and a small angular variation of 0.56 nm/deg. In experiments, we choose the sensor design in Figure 4b for the demonstration of soil moisture sensing because of its relatively small fwhm compared with other angle-independent optical sensors (Figure S7) and the accessibility of its nearinfrared operation wavelength for measurement in our reflectance apparatus.

We further show a route for the large-area, solution-based fabrication of plasmonic lattice arrays on free-standing hydrogel films (Figure S12 and details in the Experimental Section). Colloidal Au nanocrystal-based NR arrays, which possess similar LSPRs as evaporated Au NR arrays, are demonstrated using our previously reported solution-based nanoimprinting processes. 42 The uniformly patterned colloidal Au nanocrystalbased NR arrays are fabricated on the centimeter scale on hydrogel films (Figures S13 and S14) and provide a promising route to fabricate large-area, low-cost optical moisture sensors.

3. CONCLUSION

We design and demonstrate an eco-friendly optical moisture sensor with strong, angle-independent plasmonic resonances that can be useful for environmental monitoring on rough soil surfaces. We illustrate the relationship between the angular variation of the plasmonic sensor and the dimensions of the Au NR lattice array, based on which we demonstrate off-resonance optical sensors with a resonance that shifts 0.4 nm per 1 wt % soil moisture variation and that is invariant as it is tilted between angles of $0^{\circ}-13^{\circ}$. It is worth to mention that although we use the array of Au nanodot (200 nm diameter) to demonstrate the detection of soil moisture, rectangular-shaped Au NR arrays can also be designed to possess angleindependent resonances and therefore be suitable for sensing on rough surface of soil (Figure 3d). By fabricating arrays of Au NRs with angle-independent resonances operating at different wavelengths and by using various adaptive polymers, the optical sensor platform established here would allow for multiparameter testing of soil water, temperature, pH, and ionic strength, important to improving agricultural productivity. Furthermore, in the future, we will explore tailoring the shape of the nanostructures as a route to achieve higher sensor resolution/sensitivity. In addition, the sensor response rate is analyzed by an analytical model and demonstrated to be within minutes, which is at reasonable time scale for agricultural usage where the soil moisture information is collected on a daily basis or longer. Developing low-cost, angle-independent optical moisture sensors that could be distributed across fields and imaged with hyperspectral cameras found on drones provides new opportunities for smart soil moisture monitoring to tackle the challenge of water scarcity in agriculture.

4. EXPERIMENTAL SECTION

Materials. 2-Hydroxyethyl methacrylate (97%), acrylic acid (99%), ethylene glycol dimethacrylate (98%), 2-hydroxy-2-methylpropiophenone (97%), gold etchant, 3-(trimethoxysilyl)propyl methacrylate (98%), oleylamine (further referred to as OAm, 70%), and tert-butylamine-borane (TBAB, 97%) are purchased from Sigma-Aldrich. (Tridecafluoro-1,1,2,2-tetrahydrooctyl)trichlorosilane is purchased from Gelest Co. Hydrogen tetrachloroaurate(III) hydrate (99.9%) is purchased from Strem Chemicals. 1,2,3,4-Tetrahydronaphthalene (tetralin) and ammonium thiocyanate (SCN, 99+%) are

purchased from Acros. Chromium pellets (Cr, 99.999%) are purchased from Kurt J. Lesker. Gold pellets (Au 99.9999%) are purchased from APMEX. Poly(methyl methacrylate) (PMMA) 495 A4, PMMA 950 A2, anisole (99%), methyl isobutyl ketone (MIBK), and Remover PG are purchased from MicroChem. Acetone (99.8%), isopropanol (IPA) (99.5%), hexane (99.9%), and microscope slides are purchased from Fisher Scientific. The commercial humidity sensor is purchased from Amazon (Supco DVTH data view temperature and humidity data logger with display, ASIN: B0019DYB70).

Synthesis of Hydrogel Precursor. To prepare the hydrogel precursor, 200 µL of acrylic acid, 2 mL of 2-hydroxyethyl methacrylate, and 30 μ L of the photoinitiator 2-hydroxy-2-methylpropiophenone are mixed in a glass vial. The mixture is then exposed to UV light (365 nm, 97435 Oriel Flood Exposure Source, Newport Corp.) three times at a dosage of 500 mJ/cm² each time to partially polymerize the monomers. An additional 20 µL of 2-hydroxy-2-methylpropiophenone and 40 μ L of the cross-linker, ethylene glycol dimethacrylate, are added into the mixture to form the hydrogel precursor. In the synthetic hydrogel, the polymerized 2-hydroxyethyl methacrylate provides good mechanical stability, and the polymerized acrylic acid provides large water absorbability. We choose the ratio of 1:10 (2hydroxyethyl methacrylate:acrylic acid) in the synthesis of hydrogel precursor to achieve both good mechanical stability and large water absorbability for the final synthetic hydrogel. The ratio between the 2hydroxyethyl methacrylate and acrylic acid in the precursor synthesis could be further adjusted for degradable optical moisture sensors.

Fabrication of the Au NR Lattice Array. A 2 cm \times 2 cm microscope slide is cleaned by acetone and IPA using sonication for 5 min for each solution. It is followed by an O₂ plasma (75 mTorr, 150 W) cleaning for 10 min. The electron-beam lithography resist PMMA 495 A4 (dilute to A2 in anisole) is deposited by spin-coating at 3000 rpm for 1 min, prebaked at 180 °C for 2 min, and allowed to cool to room temperature for 2 min. A second resist layer of PMMA 950 A2 is then deposited following the same procedure. The total resist thickness is about 240 nm. Then 12 nm Au is deposited onto the sample at a rate of 0.2 Å/s by thermal evaporation. The NR pattern is then exposed in an Elionix electron-beam lithography system operating at a 50 kV accelerating voltage. After exposure, the Au thin film is removed in Au etchant solution for 1 min. The sample is developed in a 1:3 solution of MIBK and IPA for 90 s. Residual resist is removed by descumming in an O2 plasma (75 mTorr, 70 W) for 6 s. A 2 nm chromium adhesion layer and a 30 nm Au layer are deposited onto the sample in sequence using electron-beam evaporation, and then the sample is soaked in remover PG at 75 °C for 8 h to complete the lift-off process.

Fabrication of the Hydrogel-Coated, Au NR Array Optical Moisture Sensor. The Au NR array fabricated on a microscope slide is exposed to 3-(trimethoxysilyl)propyl methacrylate vapor for 30 min to form an ultrathin layer (approximately several nanometers) of the molecule as an anchor for the subsequently deposited hydrogel. Hydrogel precursor is spin-coated onto the Au NR array to form 640 nm thin films and by drop-casting between glass plates separated by a spacer to form 150 and 600 μ m films. Then it is kept in a transparent plastic container filled with N₂ and exposed to 2000 mJ/cm² of UV light (365 nm, 97435 Oriel Flood Exposure Source, Newport Corp.). The hydrogel film thickness of 640 nm is measured by AFM as shown in Figure S1d,e, and the films of 150 and 600 μ m thickness are measured with calipers. The cured hydrogel-coated, Au NR array optical moisture sensor is soaked in DI water (pH = 6) for 12 h to dissolve any remaining acid and un-cross-linked hydrogel monomers. For all the DI water used in the experiments, the pH is kept at 6 by dissolving pH buffer in DI water to a 60 mg/mL concentration in order to keep the same ionic strength for all sensor measurements. Although the hydrogel we use in the experiments is sensitive to pH variations, it could be further improved to be pH insensitive by replacing the acrylic acid in hydrogel with other noncharged materials such as acrylamide to prevent possible pH interferences.

FDTD Simulations. The water weight percentage in hydrogel right after soaking is 47.4%, which gives an effective RI of 1.39 assuming that water is uniformly distributed inside hydrogel. The hydrogel film

at 30% RH has about 5% water weight percentage, and we use RI = 1.44 for simulation. FDTD simulations are carried out in Lumerical simulation software for Au NR arrays on a glass substrate (n = 1.45)for a variety of NR lengths and pitches, with a fixed NR width of 200 nm and fixed NR thickness of 32 nm. Hydrogel layers of varying RIs are set on top of the Au NR arrays with semi-infinite thickness. The incident light source is set within the hydrogel layer to avoid the possible interference effects and is linear polarized along the longitudinal direction of the NRs. For angle-dependent simulations, the incident light is tilted to different angles between 0° and 15° along the longitudinal direction of the NRs.

AFM Measurement. AFM measurements are performed using an MFP-3D-BIO microscope (Asylum Research Corp.) with an AC240TS silicon cantilever (Olympus).

SEM Measurement. SEM measurements are performed using an FEI Quanta 600 ESEM. The environmental mode is used to characterize the sample on a glass substrate.

Transmittance Measurement. The transmittance spectra of the optical moisture sensors are measured using a Cary 5000 UV-vis-NIR spectrophotometer (formerly Varian Inc., now Agilent Technologies) at normal incidence. A transparent glass chamber of 2.5 L volume is used to cover the sample during measurements. A 0-24 mL volume of water is placed in the glass chamber to create different RH environments. The spectra are reported after subtraction of a background consisting of a blank substrate.

FTIR Measurement. Transmittance FTIR measurements are performed on a Nicolet 6700 (Thermo Scientific) spectrometer with a mercury cadmium telluride detector at normal incidence. The spectra are reported after background subtraction using a blank substrate.

Reflectance Measurement. Reflectance measurements are performed on a modified Olympus BX51 microscope. Under white light illumination from a halogen lamp, reflected light from the sample is collected by a NIR-optimized objective lens (Olympus LCPLN50XIR, NA 0.65) and routed by a 100 μ m core optical fiber (M43L05, Thorlabs) to a Princeton Instruments Tri-Vista 555 spectrometer equipped with a PIXIS-256E Si 2D array detector and an OMA-V InGaAs linear array detector for visible and NIR measurement, respectively. A square protected gold mirror (PFSQ20-03-M01, Thorlabs) is first put on the microscope stage as a perfect reflector to acquire the lamp spectrum. The sensor is placed upside down on soil so its hydrogel film is in contact with soil surface to facilitate the detection of moisture. After 1 h the sensor with soil underneath it is put on the microscope stage, and three measurements are taken. The sensor spectra are reported after dividing by the lamp spectrum.

Gold Nanocrystal Synthesis. The 5 nm gold nanocrystals are synthesized using a previously reported method. 42 200 mg of hydrogen tetrachloroaurate(III) hydrate, 10 mL of OAm, and 10 mL of tetralin are mixed at room temperature. The mixture is magnetically stirred under a nitrogen flow for 5 min. 1 mmol of tert-butylamine-borane (Aldrich) is dissolved in 1 mL of OAm and 1 mL of tetralin by sonication and then injected into the precursor solution. The solution changes color to deep red in 5 s. The solution is allowed to react for 1 h at room temperature, and then 60 mL of acetone is added to precipitate the Au nanocrystals. The Au nanocrystals are collected by centrifugation (8000 rpm, 6 min), washed twice with ethanol, and then dispersed in hexanes, and an additional time just prior to NR array fabrication.

Fabrication of the Colloidal Au Nancocrystal-Based NR Array on Hydrogel. Colloidal Au nanocrystal-based NR arrays are first fabricated on microscope slides via nanoimprint lithography and solution-based deposition of nanocrystals using a previously reported method.⁴² The substrate is cleaned with acetone and IPA. NXR-1000 thermal imprint resist is deposited by spin-coating onto the substrate at 3000 rpm for 1 min and is prebaked at 155 °C for 5 min. The master template consisting of a NR array pattern is placed on top of the substrate. The master template, thermal resist, and substrate stack are heated to 133 °C, compressed at 350 psi for 5 min 30 s, and then cooled to room temperature in a Nanonex NX-2600 nanoimprint tool. The template is then carefully detached from the substrate by hand.

An oxygen plasma descum process (75 mTorr, 70 W, 6 s) is performed to remove the residual layer in the imprinted area. The Au nanocrsytal dispersion (concentration varying from 10 to 20 mg/mL) is deposited by spin-coating on the resist patterned substrate at 1000 rpm for 30 s. The resist is lifted off in acetone for 30 s. Finally, ligand exchange is carried out by immersing samples into 1% NH₄SCN in acetone for 2 min, followed by rinsing twice in clean acetone for 2 min to remove unbound ligand. Hydrogel precursor is drop-cast onto the colloidal Au nanocrystal-based NR array and covered with another slide with a spacer in between to form thick film (1 mm). The cover glass slide is pretreated with (tridecafluoro-1,1,2,2-tetrahydrooctyl)trichlorosilane vapor for 1 h to create a hydrophobic surface before use. Then it is kept in a transparent plastic container filled with N2 and exposed to 2000 mJ/cm² of UV light (365 nm, 97435 Oriel Flood Exposure Source, Newport Corp.). The cured hydrogel is soaked in DI water for 12 h to release it from the microscope slide substrate with colloidal Au nanocrystal-based NR array embedded in the hydrogel surface.

ASSOCIATED CONTENT

S Supporting Information

The Supporting Information is available free of charge on the ACS Publications website at DOI: 10.1021/acsanm.8b00268.

Experimental methods, derivation of analytical model, additional fitting details, additional AFM images, additional SEM images, additional transmittance and reflectance measurements of the sensor, additional FDTD simulations, instrument setup (PDF)

AUTHOR INFORMATION

Corresponding Author

*E-mail: kagan@seas.upenn.edu (C.R.K.).

ORCID ®

Wenxiang Chen: 0000-0003-1022-9514 Gaoxiang Wu: 0000-0002-1158-9792

Nicholas J. Greybush: 0000-0001-5784-654X

Shu Yang: 0000-0001-8834-3320 Cherie R. Kagan: 0000-0001-6540-2009

Notes

The authors declare no competing financial interest.

ACKNOWLEDGMENTS

We thank Dr. J. Kikkawa for his help with reflectance measurements. We thank Daniel Straus for insightful discussions. The authors are grateful for primary support of this work from the National Science Foundation (NSF) under Award CMMI-1562884 for Au NR fabrication, atomic force and scanning electron microscopy, and moisture-dependent transmittance and reflectance measurements and analysis. Hydrogel synthesis and deposition were supported by NSF/DMR/Polymer program, DMR-1410253. Scanning electron microscopy was performed in facilities supported by the NSF MRSEC Program under Award DMR-1120901. Jordan P. Howard-Jennings' work on optical measurement is supported by NSF SUNFEST—Summer Undergraduate Research in Sensor Technologies—REU Award No. 1359107.

REFERENCES

- (1) Food and Agriculture Organization. Coping with Water Scarcity An Action Framework for Agriculture and Food Security; 2012; pp 1–78
- (2) Food and Agriculture Organization. Water Withdrawal by Sector, around 2010; 2016; pp 1–2.

- (3) Topp, G. C.; Davis, J. L.; Annan, A. P. Electromagnetic Determination of Soil Water Content: Measurements in Coaxial Transmission Lines. *Water Resour. Res.* 1980, 16, 574–582.
- (4) Robinson, D. A.; Jones, S. B.; Wraith, J. M.; Or, D.; Friedman, S. P. A Review of Advances in Dielectric and Electrical Conductivity Measurement in Soils Using Time Domain Reflectometry. *Vadose Zone J.* 2003, 2, 444.
- (5) Blonquist, J. M., Jr.; Jones, S. B.; Robinson, D. A. A Time Domain Transmission Sensor with TDR Performance Characteristics. *J. Hydrol.* **2005**, *314*, 235–245.
- (6) Qu, W.; Bogena, H. R.; Huisman, J. A.; Vereecken, H. Calibration of a Novel Low-Cost Soil Water Content Sensor Based on a Ring Oscillator. *Vadose Zone J.* **2013**, *12*, 1–37.
- (7) Muñoz-Carpena, R.; Shukla, S.; Morgan, K. Field Devices for Monitoring Soil Water Content; 2004; Vol. 343, pp 1-24.
- (8) Yu, X.; Wu, P.; Han, W.; Zhang, Z. A Survey on Wireless Sensor Network Infrastructure for Agriculture. *Comput. Stand. Interfaces* **2013**, 35, 59–64.
- (9) Ruiz-Garcia, L.; Lunadei, L.; Barreiro, P.; Robla, I. A Review of Wireless Sensor Technologies and Applications in Agriculture and Food Industry: State of the Art and Current Trends. *Sensors* **2009**, *9*, 4728–4750.
- (10) Vereecken, H.; Huisman, J. A.; Pachepsky, Y.; Montzka, C.; van der Kruk, J.; Bogena, H.; Weihermüller, L.; Herbst, M.; Martinez, G.; Vanderborght, J. On the Spatio-Temporal Dynamics of Soil Moisture at the Field Scale. *J. Hydrol.* **2014**, *516*, 76–96.
- (11) Barry, R. A.; Wiltzius, P. Humidity-Sensing Inverse Opal Hydrogels. *Langmuir* **2006**, 22, 1369–1374.
- (12) Yin, S.; Wang, C.; Liu, S.; Chen, S. Facile Fabrication of Tunable Colloidal Photonic Crystal Hydrogel Supraballs toward a Colorimetric Humidity Sensor. *J. Mater. Chem. C* **2013**, *1*, 4685–4690.
- (13) Tian, E.; Wang, J.; Zheng, Y.; Song, Y.; Jiang, L.; Zhu, D. Colorful Humidity Sensitive Photonic Crystal Hydrogel. *J. Mater. Chem.* **2008**, *18*, 1116–1122.
- (14) Islam, M. R.; Xie, S.; Huang, D.; Smyth, K.; Serpe, M. J. Poly (N-Isopropylacrylamide) Microgel-Based Optical Devices for Humidity Sensing. *Anal. Chim. Acta* **2015**, 898, 101–108.
- (15) Shi, J.; Hsiao, V. K. S.; Walker, T. R.; Huang, T. J. Humidity Sensing Based on Nanoporous Polymeric Photonic Crystals. *Sens. Actuators, B* **2008**, *129*, 391–396.
- (16) Wang, L.; Liu, Y.; Zhang, M.; Tu, D.; Mao, X.; Liao, Y. A Relative Humidity Sensor Using a Hydrogel-Coated Long Period Grating. *Meas. Sci. Technol.* **2007**, *18*, 3131–3134.
- (17) Xuan, R.; Wu, Q.; Yin, Y.; Ge, J. Magnetically Assembled Photonic Crystal Film for Humidity Sensing. *J. Mater. Chem.* **2011**, *21*, 3672–3676.
- (18) Hu, H.; Chen, Q.-W.; Cheng, K.; Tang, J. Visually Readable and Highly Stable Self-Display Photonic Humidity Sensor. *J. Mater. Chem.* **2012**, *22*, 1021–1027.
- (19) Larsson, E. M.; Langhammer, C.; Zoric, I.; Kasemo, B. Nanoplasmonic Probes of Catalytic Reactions. *Science* **2009**, 326, 1091–1094.
- (20) Mesch, M.; Zhang, C.; Braun, P. V.; Giessen, H. Functionalized Hydrogel on Plasmonic Nanoantennas for Noninvasive Glucose Sensing. *ACS Photonics* **2015**, *2*, 475–480.
- (21) Kozlovskaya, V.; Kharlampieva, E.; Khanal, B. P.; Manna, P.; Zubarev, E. R.; Tsukruk, V. V. Ultrathin Layer-by-Layer Hydrogels with Incorporated Gold Nanorods as pH-Sensitive Optical Materials. *Chem. Mater.* **2008**, *20*, 7474–7485.
- (22) Ye, S.; Zhang, X.; Chang, L.; Wang, T.; Li, Z.; Zhang, J.; Yang, B. High-Performance Plasmonic Sensors Based on Two-Dimensional Ag Nanowell Crystals. *Adv. Opt. Mater.* **2014**, *2*, 779–787.
- (23) Wang, H.; Wang, X.; Yan, C.; Zhao, H.; Zhang, J.; Santschi, C.; Martin, O. J. F. Full Color Generation Using Silver Tandem Nanodisks. ACS Nano 2017, 11, 4419–4427.
- (24) Pi, S.; Zeng, X.; Zhang, N.; Ji, D.; Chen, B.; Song, H.; Cheney, A.; Xu, Y.; Jiang, S.; Sun, D.; Song, Y.; Gan, Q. Dielectric-Grating-Coupled Surface Plasmon Resonance From the Back Side of the Metal Film for Ultrasensitive Sensing. *IEEE Photonics J.* **2016**, *8*, 1–7.

- (25) Otte, M. A.; Sepúlveda, B.; Ni, W.; Juste, J. P.; Liz-Marzán, L. M.; Lechuga, L. M. Identification of the Optimal Spectral Region for Plasmonic and Nanoplasmonic Sensing. *ACS Nano* **2010**, *4*, 349–357.
- (26) Wei, H.; Hossein Abtahi, S. M.; Vikesland, P. J. Plasmonic Colorimetric and SERS Sensors for Environmental Analysis. *Environ. Sci.: Nano* **2015**, *2*, 120–135.
- (27) Luechinger, N. A.; Loher, S.; Athanassiou, E. K.; Grass, R. N.; Stark, W. J. Highly Sensitive Optical Detection of Humidity on Polymer/Metal Nanoparticle Hybrid Films. *Langmuir* **2007**, 23, 3473—3477.
- (28) Qi, Z.; Honma, I.; Zhou, H. Humidity Sensor Based on Localized Surface Plasmon Resonance of Multilayer Thin Films of Gold Nanoparticles Linked with Myoglobin. *Opt. Lett.* **2006**, *31*, 1854—1856.
- (29) Wang, P.; Zhang, L.; Xia, Y.; Tong, L.; Xu, X.; Ying, Y. Polymer Nanofibers Embedded with Aligned Gold Nanorods: A New Platform for Plasmonic Studies and Optical Sensing. *Nano Lett.* **2012**, *12*, 3145–3150.
- (30) Kunstmann-Olsen, C.; Belić, D.; Bradley, D. F.; Grzelczak, M. P.; Brust, M. Humidity-Dependent Reversible Transitions in Gold Nanoparticle Superlattices. *Chem. Mater.* **2016**, *28*, 2970–2980.
- (31) Haes, A. J.; Stuart, D. A.; Nie, S.; Van Duyne, R. P. Using Solution-Phase Nanoparticles, Surface-Confined Nanoparticle Arrays and Single Nanoparticles as Biological Sensing Platforms. *J. Fluoresc.* **2004**, *14*, 355–367.
- (32) Guo, L.; Jackman, J. A.; Yang, H.; Chen, P.; Cho, N.; Kim, D. Strategies for Enhancing the Sensitivity of Plasmonic Nanosensors. *Nano Today* **2015**, *10*, 213–239.
- (33) Wang, T.; Yu, Y.; Chen, D.; Wang, S.; Zhang, X.; Li, Y.; Zhang, J.; Fu, Y. Naked Eye Plasmonic Indicator with Multi-Responsive Polymer Brush as Signal Transducer and Amplifier. *Nanoscale* **2017**, *9*, 1925–1933.
- (34) McMahon, J. M.; Henzie, J.; Odom, T. W.; Schatz, G. C.; Gray, S. K. Tailoring the Sensing Capabilities of Nanohole Arrays in Gold Films with Rayleigh Anomaly-Surface Plasmon Polaritons. *Opt. Express* **2007**, *15*, 18119–18129.
- (35) Kravets, V. G.; Schedin, F.; Grigorenko, A. N. Extremely Narrow Plasmon Resonances Based on Diffraction Coupling of Localized Plasmons in Arrays of Metallic Nanoparticles. *Phys. Rev. Lett.* **2008**, *101*, 087403.
- (36) Ye, J.; Van Dorpe, P. Improvement of Figure of Merit for Gold Nanobar Array Plasmonic Sensors. *Plasmonics* **2011**, *6*, 665–671.
- (37) Zambov, L. M.; Popov, C.; Abedinov, N.; Plass, M. F.; Kulisch, W.; Gotszalk, T.; Grabiec, P.; Rangelow, I. W.; Kassing, R. Gas-Sensitive Properties of Nitrogen-Rich Carbon Nitride Films. *Adv. Mater.* **2000**, *12*, 656–660.
- (38) Li, Y.; Tanaka, T. Kinetics of Swelling and Shrinking of Gels. *J. Chem. Phys.* **1990**, 92, 1365–1371.
- (39) Peppas, N. A.; Hilt, J. Z.; Khademhosseini, A.; Langer, R. Hydrogels in Biology and Medicine: From Molecular Principles to Bionanotechnology. *Adv. Mater.* **2006**, *18*, 1345–1360.
- (40) Rayleigh, Lord On the Dynamical Theory of Gratings. Proc. R. Soc. London, Ser. A 1907, 79, 399-416.
- (41) Filion, R.; Bernier, M.; Paniconi, C.; Chokmani, K.; Melis, M.; Soddu, A.; Talazac, M.; Lafortune, F.-X. Remote Sensing for Mapping Soil Moisture and Drainage Potential in Semi-Arid Regions: Applications to the Campidano Plain of Sardinia. *Sci. Total Environ.* **2016**, 543, 862–876.
- (42) Chen, W.; Tymchenko, M.; Gopalan, P.; Ye, X.; Wu, Y.; Zhang, M.; Murray, C. B.; Alu, A.; Kagan, C. R. Large-Area Nanoimprinted Colloidal Au Nanocrystal-Based Nanoantennas for Ultrathin Polarizing Plasmonic Metasurfaces. *Nano Lett.* **2015**, *15*, 5254–5260.
- (43) Nagar, R.; Vinayan, B. P.; Samantaray, S. S.; Ramaprabhu, S. Recent Advances in Hydrogen Storage Using Catalytically and Chemically Modified Graphene Nanocomposites. *J. Mater. Chem. A* **2017**, *5*, 22897–22912.
- (44) Murray, L. J.; Dincă, M.; Long, J. R. Hydrogen Storage in Metal-organic Frameworks. *Chem. Soc. Rev.* **2009**, 38, 1294–1314.

(45) Gaster, R. S.; Xu, L.; Han, S.; Wilson, R. J.; Hall, D. A.; Osterfeld, S. J.; Yu, H.; Wang, S. X. Quantification of Protein Interactions and Solution Transport Using High-Density GMR Sensor Arrays. *Nat. Nanotechnol.* **2011**, *6*, 314–320.